# LETTER

# Real-time observation of interfering crystal electrons in high-harmonic generation

M. Hohenleutner[1]*, F. Langer[1]*, O. Schubert[1]*, M. Knorr[1], U. Huttner[2]*, S. W. Koch[2], M. Kira[2] & R. Huber[1]

**Acceleration and collision of particles has been a key strategy for exploring the texture of matter. Strong light waves can control and recollide electronic wavepackets, generating high-harmonic radiation that encodes the structure and dynamics of atoms and molecules and lays the foundations of attosecond science[1–3]. The recent discovery of high-harmonic generation in bulk solids[4–6] combines the idea of ultrafast acceleration with complex condensed matter systems, and provides hope for compact solid-state attosecond sources[6–8] and electronics at optical frequencies[3,5,9,10]. Yet the underlying quantum motion has not so far been observable in real time. Here we study high-harmonic generation in a bulk solid directly in the time domain, and reveal a new kind of strong-field excitation in the crystal. Unlike established atomic sources[1–3,9,11], our solid emits high-harmonic radiation as a sequence of subcycle bursts that coincide temporally with the field crests of one polarity of the driving terahertz waveform. We show that these features are characteristic of a non-perturbative quantum interference process that involves electrons from multiple valence bands. These results identify key mechanisms for future solid-state attosecond sources and next-generation light-wave electronics. The new quantum interference process justifies the hope for all-optical band-structure reconstruction and lays the foundation for possible quantum logic operations at optical clock rates.**

Ultrafast time resolution in the few-femtosecond or attosecond regime has provided systematic insight into quantum control of individual atoms[12], molecules[13], and solids[14]. A spectacular example has been to utilize the carrier wave of strong light pulses to control subcycle electron motion in atoms and molecules and follow the wavepacket dynamics directly via the temporal structure of high-order harmonic (HH) emission[1–3,11,15]. Quantum theories[16] suggest, for example, that maximum HH emission occurs at a distinct delay after the crest of the driving field, reflecting the time needed to accelerate electrons in the continuum[16,17]. Subcycle resolution has also been used to unravel novel interference phenomena in molecules[15,18,19].

In comparison, subcycle control of electrons in solids is still in its infancy, despite its promise of novel quantum physics[4–7,10,20–23] and applications in all-optical band-structure reconstruction[22,23], light-wave-driven electronics[3,5,9,10,24] or attosecond science[6–8]. Only recently high-harmonic generation (HHG) has been extended to bulk solids, setting bandwidth records in the terahertz-to-ultraviolet spectral window[4,5]. An intriguing interplay of coherent interband polarization and intraband electron acceleration in the regime of dynamical Bloch oscillations has been suggested to underlie HHG in bulk crystals[5,7,20–23]; such a process can explain, for example, the observed linear scaling of the HH cut-off frequency with the driving peak field[4,5], in contrast to a quadratic behaviour found in atoms and molecules. A detailed understanding of the microscopic electron motion as well as all envisaged applications depends critically on direct access to the temporal structure of HHs from bulk crystals[6,23,25], which has been elusive.

Here we resolve the temporal fine structure of terahertz-driven phase-locked HH pulses from a bulk semiconductor. In addition, we directly measure the HH timing with respect to the driving field on the same absolute timescale for the first time. Our data reveal that the radiation is emitted as a train of almost bandwidth-limited bursts synchronized with the maxima of the field. Differently from atoms, the bursts are emitted only during every second half-cycle. We show that these signatures originate from a new type of non-perturbative interband quantum interference involving electrons below the Fermi energy.

Multi-octave spanning HH pulses (Extended Data Fig. 1) are generated by focusing intense phase-stable multi-terahertz transients centred at a frequency of $\nu_{THz} = 33$ THz (Fig. 1a, black waveform) into a single crystal of the semiconductor gallium selenide (GaSe). To analyse the HH pulses with subcycle resolution, we introduce a novel combination of cross-correlation frequency-resolved optical gating (XFROG) and electro-optic sampling (Fig. 1a). The generated HHs and the terahertz driving field (red waveform) are superimposed with a delayed 8-fs near-infrared gate (blue waveform) and focused into a 10-μm-thick BBO (β-barium borate) crystal. Nonlinear frequency mixing simultaneously yields sum-frequency signals encoding the temporal structure of HH pulses as well as electro-optic traces of the terahertz driving waveform (see 'Experimental setup' in Methods). In this way, the relative timing of HH emission with respect to the terahertz field is determined with an uncertainty corresponding to a fraction $T/20 = 1.5$ fs of the oscillation period $T$ of the driving waveform (see 'Determination of the absolute timescale' in Methods and Extended Data Fig. 2).

Figure 1 compares the terahertz pump field (Fig. 1b, black curve) with the spectrally integrated (Fig. 1b, shaded curve) and the spectrally resolved (Fig. 1c, colour map) sum-frequency signal. A double-blind XFROG algorithm (see 'Double-blind XFROG algorithm' in Methods) allows us to retrieve the actual temporal envelopes and relative phases of both the gate and the HH pulses[26] from the sum-frequency data. The consistency of this analysis is confirmed by the excellent agreement between the measured and reconstructed two-dimensional spectrograms (Fig. 1c and d) and between the intensity envelope of the gate pulse retrieved from the spectrogram and an independent second harmonic FROG measurement (Extended Data Fig. 3). The retrieved time trace of the HH intensity $I_{HH}(t)$ contains spectral contributions from 50 to 315 THz (Extended Data Fig. 3). $I_{HH}(t)$ consists of a train of three ultrashort bursts (Fig. 1e, shaded curve) featuring three remarkable properties, as follows. (1) The maxima of $I_{HH}(t)$ and $E_{THz}(t)$ coincide within $\pm 2$ fs $= T/15$ (vertical dashed lines). This behaviour is in contrast to ballistic electron recollision models[17] where the maximum of $I_{HH}(t)$ is distinctly delayed with respect to the maximal driving field[3]. (2) Unlike in atomic HHG, $I_{HH}(t)$ is suppressed by one order of magnitude for field maxima of negative polarity. (3) The duration of the unipolar HH bursts is as short as 7 fs (full-width at half-maximum of intensity), which corresponds to a single oscillation period of the fourth harmonic order. Such pulse widths are expected only if all frequency components within the smooth spectral envelope (Extended Data Fig. 3) generated during one half-cycle of the driving field are emitted almost simultaneously. This is indeed the case as can be seen in Fig. 1c and d, where all sum-frequency components peak roughly at

[1]Department of Physics, University of Regensburg, 93040 Regensburg, Germany. [2]Department of Physics, University of Marburg, 35032 Marburg, Germany.
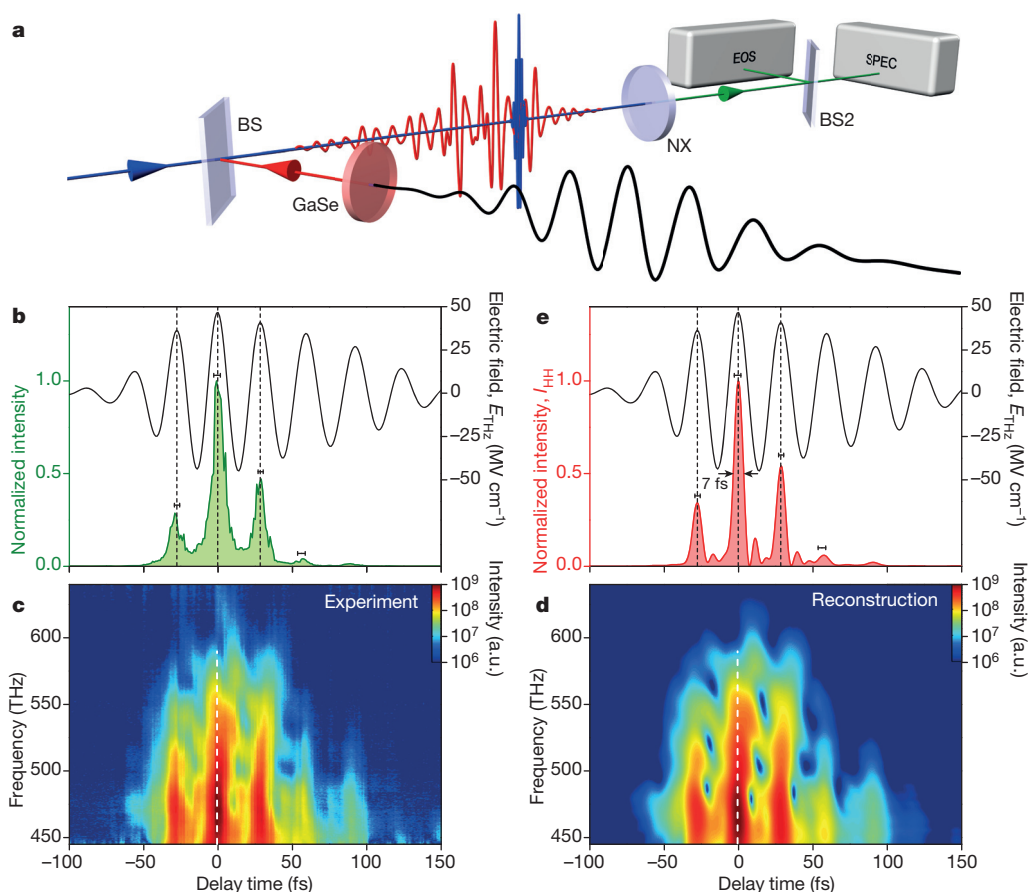*These authors contributed equally to this work.

**Figure 1 | Subcycle time structure of HH emission from a bulk crystalline solid. a**, Experimental setup of the novel cross-correlation scheme: a multi-terahertz transient (black) is focused onto a bulk GaSe crystal (thickness 60 μm) for HH generation. The resulting waveform (red) is overlapped with a near-infrared gating pulse (blue, pulse duration 8 fs, centre wavelength 840 nm) using a beam splitter (BS) and focused into a BBO crystal (NX, thickness 10 μm) for simultaneous electro-optic interaction and sum-frequency generation. These signals (green) are split with a beamsplitter (BS2) and simultaneously recorded with a standard electro-optic sampling (EOS) setup and a spectrograph with a cooled silicon CCD detector (SPEC). **b**, Waveform of the multi-terahertz driving field featuring peak amplitudes of 47 MV cm$^{-1}$ and a central frequency of 33 THz confirmed by electro-optic detection in a ZnTe

crystal (thickness 6.5 μm, black curve). Signals obtained from sum-frequency mixing of HH and gating pulses are shown after integration over a frequency window from 490 THz to 523 THz (green curve). Dashed vertical lines highlight the local maxima of the terahertz field and error bars indicate the standard deviation of the extracted sum-frequency peak position for 12 separate measurements. **c, d**, Spectrograms showing the intensity of the measured sum-frequency signal for different delay times and frequencies as recorded with a Si CCD detector (**c**) and reconstructed using a double-blind XFROG algorithm (**d**), respectively. White dashed lines highlight the maximum sum-frequency intensity. **e**, Temporal shape of intensity $I_{HH}$ (red) of the reconstructed HH pulse sequence relative to the driving multi-terahertz waveform (black). Dashed lines and error bars are the same as in **b**.

the same delay time $t$ (vertical broken line in Fig. 1c and d), suggesting, at most, a weak spectral chirp of the HH pulses.

The observed time structure implies a quasi-instantaneous and unipolar generation mechanism. In order to identify this key ingredient, we first reproduce $I_{HH}(t)$ by a full quantum theory[5,20] (see 'Quantum many-body model' in Methods) including intra- and interband dynamics with two conduction and three valence bands (Extended Data Fig. 4). Our calculation reproduces the experimentally observed behaviour of $I_{HH}(t)$ in great detail (Fig. 2a, red solid curve). In particular, the emission peaks within 2 fs about the positive field crest while it is strongly suppressed for negative field extrema. In contrast, recent models accounting for only two electronic bands have consistently predicted HH emission in a bipolar fashion[7,25] and have suggested analogies with atomic HHG[22] where mostly two classes of electronic states have been considered: the ground state and the continuum of ionized states. In a solid, however, the simultaneous interaction of each electron with many atoms of the crystal lattice forms a series of electronic bands. As soon as more than two bands are included, electrons may be excited through multiple paths inducing quantum interference.

Figure 2b illustrates a minimal model for this scenario accounting for two valence bands (h$_1$ and h$_2$) and one conduction band (e$_1$). Excitation of an electron from band h$_1$ to band e$_1$ may either proceed

by multi-photon transitions directly between two bands, h$_1 \rightarrow$ e$_1$, or indirectly via an additional band, h$_1 \rightarrow$ h$_2 \rightarrow$ e$_1$. The terahertz pulse is far off either resonance, but it is sufficiently strong to generate non-perturbative excitations where electron populations change drastically on a subcycle scale. We show that such non-perturbative transitions tend to balance the respective weights of the excitation paths because the extremely strong field forces the electrons to oscillate between the non-resonantly coupled states (see 'Interference path efficiency' in Methods). Nonetheless, the excitation paths maintain their perturbatively assigned symmetry (see 'Strong-field quantum interference' in Methods), featuring an odd transition amplitude $A_o(-E_{THz}) = -A_o(E_{THz})$ with respect to the driving field for the direct excitation and an even amplitude $A_e(-E_{THz}) = A_e(E_{THz})$ for the indirect path h$_1 \rightarrow$ h$_2 \rightarrow$ e$_1$ (Fig. 2b, Extended Data Fig. 5). A coherent superposition of both yields a total amplitude of $A_e(|E_{THz}|) + (-)$ $A_o(|E_{THz}|)$ for positive (negative) $E_{THz}$, respectively (see 'Perturbative versus non-perturbative quantum interference' in Methods). Hence, the sign of the field controls the total outcome of HH transitions. Note that the transition h$_1 \rightarrow$ h$_2$ connecting bands below the Fermi level is initially Pauli-blocked but strong excitation can significantly empty h$_2$, for example, via the transition h$_2 \rightarrow$ e$_1$, clearing the path h$_1 \rightarrow$ h$_2 \rightarrow$ e$_1$.
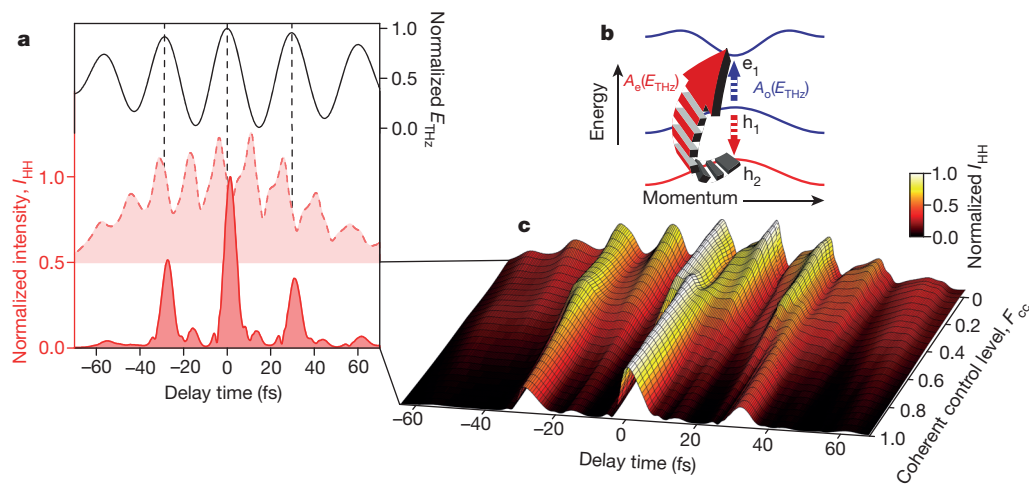
**Figure 2 | Non-perturbative quantum interference in HH emission.**
**a**, Driving terahertz field (black curve) and calculated intensity envelope of HH emission as a function of time for $F_{cc} = 0$ (broken red curve, magnified by a factor of 25) and $F_{cc} = 1$ (solid red curve). Dashed vertical lines highlight the local maxima of the terahertz field. **b**, Simplified three-band schematic of different ionization pathways from valence band $h_1$ to conduction band $e_1$. The direct transition amplitude $A_o(E_{THz})$ is an odd function of the driving field, $A_o(-E_{THz}) = -A_o(E_{THz})$. The amplitude $A_e(E_{THz})$ of the indirect path

$(h_1 \rightarrow h_2 \rightarrow e_1)$ is the product of two odd functions, resulting in even symmetry $A_e(-E_{THz}) = A_e(E_{THz})$. The indirect path features a transition $(h_1 \rightarrow h_2)$ that is initially blocked by Pauli exclusion and only opens under strong-field excitation. **c**, HH intensity envelopes computed within the five-band model as a function of delay time and the coherent control factor $F_{cc}$ regulating coherent transitions between occupied valence bands. Bright colours mark strong emission, dark colours mark weaker emission (see key). All time traces are normalized separately.

We test the viability of this concept by a systematic switch-off analysis using our five-band computation that includes all relevant transitions. By artificially multiplying the dipole moment $d_{h_1 h_2}$ between the hole bands $h_1$ and $h_2$ as well as all other similar terms with a coherent control factor $F_{cc}$, we eliminate the indirect paths needed for non-perturbative quantum interference. Figure 2a compares the intensity envelope, $I_{HH}(t)$, with (red solid line, $F_{cc} = 1$) and without (red dashed line, $F_{cc} = 0$) the indirect paths. Switching off the quantum interference, that is, considering only direct transitions ($F_{cc} = 0$), produces bursts at positive and negative crests of the field. Interestingly, the bursts become delayed by roughly $T/4$ with respect to the field extrema, which is consistent with a delay expected in an atomic recollision model[3,17]. However, opening the indirect paths ($F_{cc} = 1$) synchronizes the emission with the driving field. More specifically, the interband coherence is driven such that the quantum interference and the resulting HH emission are strongest during the presence of the electric field. This process maximizes (suppresses) the emission with the positive (negative) crests of the field. The destructive interference is not perfect, leaving small HH remnants at negative peak fields.

Figure 2c shows computed normalized $I_{HH}(t)$ traces as a function of $F_{cc}$ (unscaled representation in Extended Data Fig. 6). By gradually suppressing the coherent-control paths, emission appears as delayed bursts after each field maximum and minimum. Nevertheless, the transition is not smooth, but contains non-trivial oscillations and bifurcations. These features are caused by terahertz-induced band mixing, which modulates electronic populations and $I_{HH}(t)$ and underpins the non-perturbative character of the interband excitations.

Under the extremely non-resonant conditions of our experiment ($h\nu_{THz} < E_g/14$ with $E_g = 2.0$ eV being the bandgap energy of GaSe), band-to-band transitions require multi-terahertz pump photons. Non-perturbative excitations can non-resonantly drive all these transitions to exhibit large population transfer (Extended Data Fig. 5), and the related processes are robust against variations of the terahertz field strength and photon energy. Therefore, the quantum interference should be detectable for a broad range of field amplitudes $E_{THz}$ and terahertz photon energies. In fact, the HH maxima remain synchronized with the positive peak of the driving field for both experimental (Fig. 3a) and theoretical (Fig. 3b) traces of $I_{HH}(t)$ when the terahertz frequency is changed between 25 and 34 THz, whereas the temporal separation of the emission bursts grows with the oscillation period of the driving field. Both measured (Fig. 3c)

and computed (Fig. 3d) traces of $I_{HH}(t)$ also remain unipolar and quasi-instantaneous when the terahertz field amplitude $E_{THz}$ is changed. The contrast is even enhanced for higher field strengths.

Recent studies have demonstrated that strong terahertz fields, needed to create HH emission, can also coherently accelerate electrons throughout the Brillouin zone before scattering occurs[4–6,21,27]. Owing to resulting dynamical Bloch oscillations, electrons may undergo one or more Bragg reflections within one half-cycle of the driving field, emitting high-frequency radiation at the quasi-instantaneous Bloch frequency $\nu_B$. Since $\nu_B$ is proportional to $E_{THz}$ (see ref. 28), the frequency of the Bloch-related contribution to HHG should trace the temporal profile of the driving field. Our XFROG algorithm allows us to retrieve the temporal phase $\phi_{HH}(t)$ of the HH pulse train (Extended Data Fig. 7), from which we obtain its instantaneous frequency $\nu_i(t) = (2\pi)^{-1}\partial\phi_{HH}/\partial t$, weighted by the spectral amplitude within our detection bandwidth (Fig. 3e). All time traces of $\nu_i(t)$ measured for different terahertz amplitudes follow a universal double-chirp pattern, which is a fingerprint of dynamical Bloch oscillations: after a monotonic increase during the rising slope of $E_{THz}(t)$, $\nu_i$ peaks approximately at the maximum of the applied field and decreases again following the abating driving field. With increasing amplitude, the instantaneous frequency in a single HH pulse blue-shifts globally while its maximum broadens, develops shoulders and finally morphs into a non-monotonic pattern for the highest field strengths. Our quantum theory reproduces even these non-trivial features well (Fig. 3f).

The combination of non-perturbative quantum interference and dynamical Bloch oscillations may be systematically harnessed for ultrashort pulse shaping. By varying the terahertz carrier frequency (Fig. 3a, b) and the carrier-envelope phase (CEP) of the driving waveform (Extended Data Fig. 8), the global shape of the HH pulse sequence can be tailored, whereas the frequency modulation within individual bursts is reproducibly set by the terahertz amplitude. Almost bandwidth-limited pulses may be generated—especially if the phase-flattening effect for high peak fields is exploited (Fig. 3e, f). We expect that in our experiment, suitable high-pass filtering of the HH pulses may allow for pulse durations as short as 3 fs in the infrared and visible domain (Extended Data Fig. 9). Since the principle of solid-based HHG is fully scalable to the ultraviolet, even shorter pulses may be possible in wide-gap materials.

In conclusion, the relative timing of HHG with respect to the driving field, the unipolar response, and a non-monotonic frequency modulation
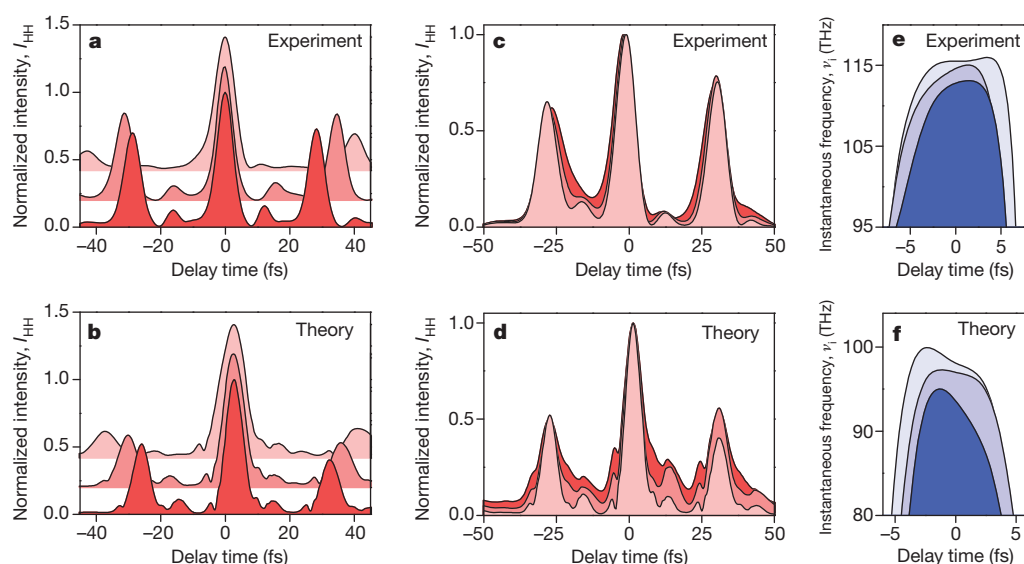
**Figure 3 | Tunability and robustness of non-perturbative quantum interference. a, b**, Measured (**a**) and calculated (**b**) intensity envelopes $I_{HH}$ of emitted HH for driving fields featuring central frequencies of 25, 30 and 34 THz, respectively. Darker colours represent higher central frequencies. **c, d**, Measured (**c**) and calculated (**d**) HH intensity envelopes for driving peak fields of 26, 31 and 44 MV cm$^{-1}$ (experiment) and 19, 22 and 31 MV cm$^{-1}$ (theory). Brighter colours represent higher peak fields. **e, f**, Instantaneous frequency $\nu_i$ of the central HH emission bursts shown in **c** and **d**, respectively. Brighter colours represent higher peak fields.

provide direct insight into the terahertz strong-field-driven motion of electrons in GaSe. We identify a non-perturbative quantum interference between interband transitions as a salient HH generation mechanism. In its most generic form, this strong-field mechanism can occur if (1) there is a closed-loop triangle system of states that are all mutually coupled by dipole transitions (Extended Data Fig. 10), and (2) the terahertz field is far below these resonances and (3) strong enough to generate non-perturbative excitations changing carrier populations substantially (see Methods and Extended Data Fig. 5). In contrast to established techniques of perturbative quantum interference between one- and two-photon transitions inducing directed charge and spin currents[29], our new concept is robust even at extremely strong fields. Thus, it may inspire new techniques for quantum-logic operations[30] based on sturdy, non-perturbative transitions between strongly coupled energy bands. Driving coherences between initially fully occupied valence bands, HHG provides all-optical access even to details of the band structure hidden below the Fermi level. Furthermore, the direct observation of lightwave-controlled electron dynamics marks the way towards a complete microscopic picture of HHG in solids, ultrafast electronics, and novel solid-state CEP-stable attosecond sources.

**Online Content** Methods, along with any additional Extended Data display items and Source Data, are available in the online version of the paper; references unique to these sections appear only in the online paper.

1. Paul, P. M. *et al.* Observation of a train of attosecond pulses from high harmonic generation. *Science* **292**, 1689–1692 (2001).
2. Dudovich, N. *et al.* Measuring and controlling the birth of attosecond XUV pulses. *Nature Phys.* **2**, 781–786 (2006).
3. Krausz, F. & Stockman, M. I. Attosecond metrology: from electron capture to future signal processing. *Nature Photon.* **8**, 205–213 (2014).
4. Ghimire, S. *et al.* Observation of high-order harmonic generation in a bulk crystal. *Nature Phys.* **7**, 138–141 (2011).
5. Schubert, O. *et al.* Sub-cycle control of terahertz high-harmonic generation by dynamical Bloch oscillations. *Nature Photon.* **8**, 119–123 (2014).
6. Ghimire, S. *et al.* Strong-field and attosecond physics in solids. *J. Phys. B* **47**, 204030 (2014).
7. Higuchi, T., Stockman, M. I & Hommelhoff, P. Strong-field perspective on high-harmonic radiation from bulk solids. *Phys. Rev. Lett.* **113**, 213901 (2014).
8. Mücke, O. D. Isolated high-order harmonics pulse from two-color-driven Bloch oscillations in bulk semiconductors. *Phys. Rev. B* **84**, 081202 (2011).
9. Goulielmakis, E. *et al.* Attosecond control and measurement: lightwave electronics. *Science* **317**, 769–775 (2007).
10. Zaks, B., Liu, R. B. & Sherwin, M. S. Experimental observation of electron–hole recollisions. *Nature* **483**, 580–583 (2012).
11. Shafir, D. *et al.* Resolving the time when an electron exits a tunnelling barrier. *Nature* **485**, 343–346 (2012).
12. Drescher, M. *et al.* Time-resolved atomic inner-shell spectroscopy. *Nature* **419**, 803–807 (2002).
13. Calegari, F. *et al.* Ultrafast electron dynamics in phenylalanine initiated by attosecond pulses. *Science* **346**, 336–339 (2014).
14. Neppl, S. *et al.* Direct observation of electron propagation and dielectric screening on the atomic length scale. *Nature* **517**, 342–346 (2015).
15. Smirnova, O. *et al.* High harmonic interferometry of multi-electron dynamics in molecules. *Nature* **460**, 972–977 (2009).
16. Salières, P. *et al.* Feynman's path-integral approach for intense-laser-atom interactions. *Science* **292**, 902–905 (2001).
17. Corkum, P. B. Plasma perspective on strong-field multiphoton ionization. *Phys. Rev. Lett.* **71**, 1994–1997 (1993).
18. Shafir, D., Mairesse, Y., Villeneuve, D. M., Corkum, P. B. & Dudovich, N. Atomic wavefunctions probed through strong-field light-matter interaction. *Nature Phys.* **5**, 412–416 (2009).
19. Kanai, T., Minemoto, S. & Sakai, H. Quantum interference during high-order harmonic generation from aligned molecules. *Nature* **435**, 470–474 (2005).
20. Golde, D., Meier, T. & Koch, S. W. High harmonics generated in semiconductor nanostructures by the coupled dynamics of optical inter- and intraband excitations. *Phys. Rev. B* **77**, 075330 (2008).
21. Földi, P., Benedict, M. G. & Yakovlev, V. S. The effect of dynamical Bloch oscillations on optical-field-induced current in a wide-gap dielectric. *New J. Phys.* **15**, 063019 (2013).
22. Vampa, G. *et al.* Theoretical analysis of high-harmonic generation in solids. *Phys. Rev. Lett.* **113**, 073901 (2014).
23. Hawkins, P. G., Ivanov, M. Y. & Yakovlev, V. S. Effect of multiple conduction bands on high-harmonic emission from dielectrics. *Phys. Rev. A* **91**, 013405 (2015).
24. Chin, A. H., Calderón, O. G. & Kono, J. Extreme midinfrared nonlinear optics in semiconductors. *Phys. Rev. Lett.* **86**, 3292–3295 (2001).
25. Ghimire, S. *et al.* Generation and propagation of high-order harmonics in crystals. *Phys. Rev. A* **85**, 043836 (2012).
26. Sekikawa, T., Katsura, T., Miura, S. & Watanabe, S. Measurement of the intensity-dependent atomic dipole phase of a high harmonic by frequency resolved optical gating. *Phys. Rev. Lett.* **88**, 193902 (2002).
27. Kemper, A. F., Moritz, B., Freericks, J. K. & Devereaux, T. P. Theoretical description of high-order harmonic generation in solids. *New J. Phys.* **15**, 023003 (2013).
28. Zener, C. A. Theory of the electrical breakdown of solid dielectrics. *Proc. R. Soc. Lond. A* **145**, 523–529 (1934).
29. Zhao, H., Loren, E. J., van Driel, H. M. & Smirl, A. L. Coherence control of Hall charge and spin currents. *Phys. Rev. Lett.* **96**, 246601 (2006).
30. Ladd, T. D. *et al.* Quantum computers. *Nature* **464**, 45–53 (2010).

**Author Contributions** M.H., F.L., O.S., U.H., S.W.K., M. Kira and R.H. conceived the study. M.H., F.L., O.S., M. Knorr and R.H. carried out the experiment and analysed the data. U.H., S.W.K. and M. Kira developed the quantum-mechanical model and carried out the computations. M.H., F.L., O.S., U.H., S.W.K., M. Kira and R.H. wrote the manuscript. All authors discussed the results.

**Author Information** Reprints and permissions information is available at www.nature.com/reprints. The authors declare no competing financial interests. Readers are welcome to comment on the online version of the paper. Correspondence and requests for materials should be addressed to R.H. (rupert.huber@physik.uni-regensburg.de) or M. Kira (mackillo.kira@physik.uni-marburg.de).

## METHODS

**Experimental setup.** A femtosecond titanium–sapphire laser amplifier (repetition rate, 3 kHz; pulse energy, 5.5 mJ; pulse duration, 33 fs; centre wavelength, 805 nm) is used to pump two parallel dual-stage optical parametric amplifiers tunable between centre wavelengths of 1.1 μm and 1.8 μm which deliver signal pulse energies of up to 0.5 mJ each. We generate phase-locked multi-terahertz pulses via difference frequency generation between these spectrally detuned near-infrared pulse trains[31].

High-order harmonics (HHs) are obtained by focusing these intense waveforms onto a gallium selenide (GaSe) crystal. Using samples 220 μm thick, power conversion efficiencies of approximately 7% for the whole HH spectrum covering the spectral range from 45 to 675 THz are observed. Resulting pulse energies of roughly 350 nJ are measured for a peak driving field of 72 MV cm$^{-1}$ close to the observed damage threshold of GaSe. The threshold decreases for thinner samples suggesting thermal heating as the relevant damage mechanism. For the time-resolved experiments, a 60-μm-thick free-standing GaSe crystal is irradiated (centre frequency, 33 THz; electric peak field, 47 MV cm$^{-1}$; see inset Extended Data Fig. 1) under normal incidence to avoid phase matching effects. Under these conditions, the Bloch period amounts to 5.2 fs, corresponding to an energy of 0.8 eV. The polarization of the driving field points along the Γ–K direction of the hexagonal Brillouin zone of GaSe. The resulting spectrum (Extended Data Fig. 1) is recorded by means of a monochromator in combination with a calibrated pyroelectric detector (PED) and a lead sulfide (PbS) diode, as well as spectrometers with indium gallium arsenide (InGaAs) and cooled silicon (Si) detector arrays, respectively.

A YAG-based supercontinuum source with a combination of chirped mirrors and a prism compressor provides 8-fs gating pulses with a centre wavelength of 840 nm (Extended Data Fig. 3). Both the gating and the HH pulses are focused onto a 10-μm-thick β-BaB$_2$O$_4$ (BBO) crystal, which mediates two distinct nonlinear optical processes simultaneously, as follows. (1) The HHs are mixed with the gate by ultrabroadband sum-frequency generation. This cross-correlation signal is recorded as a function of the delay time $t$ between the HH and gate pulses and encodes the temporal structure of both. (2) The terahertz fundamental wave induces an electro-optic polarization rotation of the gate pulse. This signature $S_{EOS\text{-}BBO}(t)$ serves as a time marker directly linking the emitted HH intensity $I_{HH}(t)$ with the generating terahertz field $E_{THz}(t)$ (see below for details).

**Determination of the absolute timescale.** For a complete time-domain picture of high-harmonic generation (HHG) in solids, the emitted signal ($E_{HH}$) has to be measured and temporally correlated with the driving field ($E_{THz}$) with a precision significantly better than one optical cycle of $E_{THz}$. The most accurate way to determine the relative timing is to detect the co-propagating terahertz wave and the generated HHs simultaneously within the same detector. Additionally, the detector response as well as all propagation effects between HH generation and detection of the waveforms has to be taken into account.

In our experiment, we superimpose the HH waveform including the fundamental terahertz field and an ultrashort near-infrared pulse within the same 10-μm-thick BBO crystal to generate sum-frequency ($S_{SF}$) and electro-optic signals ($S_{EOS\text{-}BBO}$). This electro-optic trace is employed as a temporal reference marker only. The strong material dispersion of BBO[32] in the multi-terahertz spectral region distorts the fundamental waveform. For a faithful determination of the temporal profile of the terahertz field, we exchange the BBO crystal with a 6.5-μm-thick ⟨110⟩-oriented zinc telluride (ZnTe) sampling crystal glued on a 300-μm-thick electro-optically inactive ZnTe substrate and record the electro-optic signal ($S_{EOS\text{-}ZnTe}$) for different delay times (Extended Data Fig. 2). Via an analysis of the Gouy phase shift[33] for several recordings ('z-scan'), we ensure that the ZnTe crystal is placed in exactly the same position as the BBO crystal.

The accuracy of this correlation procedure is estimated to be 1.2 fs by repeatedly exchanging the BBO and ZnTe crystals and calculating the standard deviation of the temporal delay between the transients recorded in BBO and ZnTe detectors, respectively. The error resulting from a misalignment of the detection crystals is on the order of 0.1 fs and may be neglected.

Finally, we correct for effects of phase-matching and dispersion of the $\chi^{(2)}$ nonlinearity using standard procedures[34] (compare Extended Data Fig. 2b) to obtain the terahertz field $E_{Det}$ at the detector position for a given signal $S_{EOS\text{-}ZnTe}$. The thickness of the ZnTe crystal $d_{ZnTe}$ is confirmed by optical interference to be $d_{ZnTe} = 6.5$ μm $\pm$ 0.7 μm, resulting in an error of the peak field positions of 0.9 fs due to the uncertainty in the determination of the crystal thickness. Consequently, the relative error in the temporal delay between the sum-frequency signal ($S_{SF}$) generated by the emitted HHs and the terahertz field at the detection focus is 1.5 fs, that is, approximately 20 times shorter than one oscillation period of the terahertz waveform.

Propagation effects between HHG and detection of the fields may modify the measured signals additionally. We employ only reflective optics between the generation and detection stages. Consequently, differences in group velocities are

negligible in our experiment. The GaSe sample is placed directly in the focus of the terahertz wave, leading to an additional Gouy phase[33] offset of π/2. For our focusing conditions, the Rayleigh length of the driving terahertz beam is about 500 μm, which is much longer than the crystal thickness of 60 μm and allows us to neglect the uncertainty in the sample position. The Gouy phase shift at the detection focus is also fully accounted for.

During propagation inside the sample, dispersion of the HH group velocity would lead to a relative delay of the spectral components corresponding to different harmonic orders. Since we deliberately avoid phase-matching during HHG in GaSe, the emission of HHs is confined to a thin region near the back facet of the GaSe crystal with a coherence length of, for example, 6 μm for the 9th harmonic, and no substantial chirp due to linear material dispersion is observed in the experiment. Note that the rear facet itself does not have an essential role in HHG. The HH radiation rather originates from the bulk of the crystal, as seen from the fact that phase-matching effects occur in thicker samples[5].

**Double-blind XFROG algorithm.** For the characterization of the temporal structure of terahertz HHs, we perform cross-correlation frequency resolved optical gating[35] (XFROG) between an 8-fs gating pulse and the HH pulse train. Our analysis is based on standard XFROG algorithms[36,37], customized to take into account the ultrabroadband nature of the HH spectra. The gating pulse encompasses a spectral bandwidth of more than 100 THz (Extended Data Fig. 3), while the emitted HH spectrum continuously covers multiple optical octaves. As a consequence, ultrabroadband sum-frequency mixing signals comprise a frequency range of more than 300 THz (Extended Data Fig. 3), benefitting from the huge acceptance bandwidth of the 10-μm-thick BBO crystal. Despite the enormous bandwidths, the XFROG algorithm reliably converges for discretionary runs and data sets and reconstructs the measured spectrograms to a very high degree of congruency (compare Fig. 1). The robustness of the scheme is additionally confirmed by comparison of the retrieved temporal shape of the gating pulse to an independent SHG FROG measurement, reconstructed using a separate algorithm[38] (Extended Data Fig. 3b).

The robust XFROG reconstruction allows us to retrieve the subcycle profile of both the intensity envelope $I_{HH}(t)$ and the relative phase $\phi_{HH}(t)$ of the HH bursts. While the temporal structure of $I_{HH}(t)$ is shown in Fig. 1e, Extended Data Fig. 7 depicts the relative phase. The modulations of the phase are relatively small as already indicated by the almost simultaneous appearance of all sum-frequency spectral contributions (Fig. 1c). To study the phase evolution in greater detail, we derive the instantaneous frequency $\nu_i = (2\pi)^{-1}\partial\phi_{HH}/\partial t$ by numerical differentiation. The instantaneous frequency is ramped up during the rising edge of a HH burst, peaks together with the intensity envelope and decreases again (Extended Data Fig. 7). This slight double-chirp is an indicator of Bloch-type acceleration of carriers within the conduction band. Furthermore, the phase retrieval allows for the reconstruction of the HH field trace (compare red waveform in Fig. 1a).

**Quantum many-body model.** We use the HHG theory developed in refs 20 and 39 to describe the coherent interplay of interband excitations and intraband currents and apply this microscopic model to study the time resolved emission of GaSe excited with extremely strong terahertz fields. The numerical calculations are based on a one-dimensional five-band model as depicted in Extended Data Fig. 4a, including two conduction bands ($\lambda = e_1, e_2$, blue lines) and three valence bands ($\lambda = h_1, h_2, h_3$, red lines). The individual bands are modelled by effectively one-dimensional tight-binding bands[39], with material parameters taken from ref. 40. In the following, we will review relevant details, while more comprehensive derivations can be found in ref. 5.

The presence of a sufficiently strong external electric field $E(t)$ induces interband transitions where electrons are transferred between two different bands $\lambda$ and $\lambda'$, as schematically depicted by the blue spheres and the black arrow in Extended Data Fig. 4b. The dipole-matrix element $d_{\lambda\lambda'}$ determines the strength of the transition. The inter-valence-band dipole-matrix element $d_{h_1h_2}$ exceeds the values of $d_{h_1e_1}$ and $d_{h_2e_1}$ by one order of magnitude[41]. The strongest driving fields applied in the calculations correspond to peak Rabi energies of 1.5 eV for inter-valence-band transitions and 0.12 eV for valence-to-conduction-band transitions. In addition to the interband transitions, $E(t)$ also drives intraband currents where electrons and holes are accelerated in their respective bands[4–8,20–23,25,27,42], see Extended Data Fig. 4c.

Defining electron and hole occupations $f_k^\lambda$ and microscopic polarizations $p_k^{\lambda\lambda'}$ for $\lambda \neq \lambda'$, the well-known semiconductor Bloch equations[43] (SBEs) describe the time evolution of polarizations and carrier occupations. The SBEs read

$$\hbar\frac{\partial}{\partial t}f_k^{e_1} = -2\text{Im}\left[d_{e_1e_2}(k)E(t)p_k^{e_2e_1} + \sum_{h_\lambda}d_{e_1h_\lambda}(k)E(t)\left(p_k^{h_\lambda e_1}\right)^*\right]$$
$$+ |e|E(t)\nabla_kf_k^{e_1} + \hbar\frac{\partial}{\partial t}f_k^{e_1}\Big|_{relax} \tag{1}$$

for the carrier occupation of the first conduction band, and

$$i\hbar \frac{\partial}{\partial t} p_k^{h_i e_j} = \left( \varepsilon_k^{e_j} + \varepsilon_k^{h_i} - i\frac{\hbar}{T_2} \right) p_k^{h_i e_j} - d_{e_j h_i}(k) E(t) \left( 1 - f_k^{e_j} - f_k^{h_i} \right) + i|e|E(t)\nabla_k p_k^{h_i e_j}$$
$$+ E(t) \sum_{e_\lambda \neq e_j} \left[ d_{e_\lambda h_i}(k) p_k^{e_\lambda e_j} - d_{e_j e_\lambda}(k) p_k^{h_i e_\lambda} \right]$$
$$+ E(t) \sum_{h_\lambda \neq h_i} \left[ d_{h_\lambda h_i}(k) p_k^{h_\lambda e_j} - d_{e_j h_\lambda}(k) p_k^{h_i h_\lambda} \right] \qquad (2)$$

for the microscopic polarizations between a valence band and a conduction band. In order to capture the dominant effects of the higher-order correlations, we include a phenomenological dephasing via the decay time $T_2 = 1.1$ fs in the polarization dynamics, following refs 5 and 44.

Multi-photon coherence is particularly susceptible to dephasing because any scattering scrambles its phase relations. In fact, similarly fast decay times of coherences have been reported in different systems ranging from bandgap dynamics in silicon[45] (0.5-fs decay) via general HHG in solids (ref. 22 (4-fs decay) and ref. 46 (sub-10-fs decay)) to atomic HHG[47] (sub-10-fs decay). This ultrafast timescale results from electron–electron scattering[45] as well as polarization–polarization scattering[47], which is fostered by the broad carrier and polarization distribution created in HHG. In addition, the terahertz field excites a large amount of electrons much faster than Coulomb screening builds up. The unscreened Coulomb interaction enhances scattering rates significantly, as discussed for example, in ref. 47. The resulting dynamics are numerically solved for an initially unexcited system using an excitation field $E(t)$ modelled closely to the experimental terahertz waveform.

The emission intensity of a coherently excited semiconductor consists of a polarization source $P(t)$ and a current source $J(t)$,

$$P(t) = \sum_{\lambda, \lambda', k} d_{\lambda, \lambda'}(k) p_k^{\lambda, \lambda'} \text{ and } J(t) = \sum_{\lambda, k} j_\lambda(k) f_k^\lambda \qquad (3)$$

with the current matrix element $j_\lambda(k) = \frac{|e|}{\hbar}\nabla_k \varepsilon_k^\lambda$.

To account for the damping of currents in a realistic system, a phenomenological carrier relaxation $\hbar\frac{\partial}{\partial t}f_k^\lambda\big|_{\text{relax.}} = -\frac{1}{\tau}f_{k,A}^\lambda$ is included, which damps the antisymmetric part $f_{k,A}^\lambda = \frac{1}{2}\left[f_k^\lambda - f_{(-k)}^\lambda\right]$ of the carrier distributions, producing the correct decay for the currents. We apply this relaxation to all valence bands and the first conduction band, with the relaxation time $\tau = 7$ fs. Owing to its flat shape, the second conduction band does not contribute essentially to the currents.

The emission intensity is defined by the total effective current given by the sum of intraband currents $J(t)$ and the rate of change of the macroscopic polarization[48] $\frac{\partial}{\partial t}P(t)$,

$$E_{\text{HHG}}(t) \propto \frac{\partial}{\partial t}P(t) + J(t) \qquad (4)$$

The envelope and phase of the numerically computed time trace is extracted via a Hilbert transform[49]. As experimental evidence from phase matching effects (see 'Determination of the absolute timescale' in Methods) suggests, surface effects do not contribute considerably to the HHG and are, thus, neglected in our model.

**Strong-field quantum interference.** As described in the previous section, all our numerical analysis is performed with the five-band model. However, in order to obtain an intuitive understanding of the dominant quantum-interference paths contributing to the experimental observations, it is sufficient to consider a simplified system that includes only the three most relevant bands. As depicted in Extended Data Fig. 5a, we use two valence bands $h_1$ and $h_2$ (red solid lines) and one conduction band e (blue solid line). The transition probabilities between the bands are given by the magnitude of the dipole-matrix elements $d_{eh_1}$, $d_{eh_2}$ and $d_{h_2 h_1}$ (black arrows). For an initially unexcited system, only transitions from the two valence bands $h_1$ and $h_2$ to the conduction band e are possible, as both valence bands are completely filled, preventing any transition between them.

In order to study the different excitation paths leading to the effective transition $h_1 \to e$, the sources

$$i\hbar\frac{\partial}{\partial t}p_k^{h_1 e}\bigg|_{\text{ex.}} = -d_{eh_1}(k)E(t)(1 - f_k^e - f_k^{h_1}) + d_{h_2 h_1}(k)E(t)p_k^{h_2 e} + d_{eh_2}(k)E(t)p_k^{h_1 h_2} \qquad (5)$$

based on equation (2) are analysed for the situation of three bands depicted in Extended Data Fig. 5a. The gradient term is omitted here, because it only redistributes the carrier momentum inside a band without inducing transitions between different bands. For the sake of a simpler notation, we will also omit the explicit $k$-dependence from now on.

The first excitation path $h_1 \to e$ (first term in equation (5)) is depicted by the blue arrow in Extended Data Fig. 5b. The terahertz driving field creates a

polarization between the first valence and the conduction band, which is proportional to the driving field strength and the corresponding dipole-matrix element. We call this the direct excitation path, $p_k^{h_1 e}|_{\text{direct}} \propto d_{eh_1}E(t)$; it is initially linear in the electric field $E(t)$ and thus of odd order with respect to the driving field sign. For strong fields, this polarization will eventually excite electrons by multi-photon absorption to the conduction band. This change in the carrier occupations given by $f_k^e|_{\text{direct}} \propto d_{eh_1}E(t)(p_k^{h_1 e}|_{\text{direct}})^* \propto d_{eh_1}^2 E(t)^2$ will modulate the initially linear dependence via the electron occupations of the involved states. Nevertheless the odd symmetry of the transition is preserved: Due to the mutual coupling of polarization and carrier occupations, that is, $p_k^{h_1 e}|_{\text{direct}} \propto d_{eh_1}E(t) - d_{eh_1}E(t)f_k^e|_{\text{direct}}$ and $f_k^e|_{\text{direct}} \propto d_{eh_1}E(t)(p_k^{h_1 e}|_{\text{direct}})^* \propto d_{eh_1}^2 E(t)^2$ the initially linear dependence will be replaced by a series of terms, which are all of odd order in the driving field, that is, $p_k^{h_1 e}|_{\text{direct}} \propto d_{eh_1}E(t) - d_{eh_1}^3 E(t)^3 + \cdots$.

In the same way, the excitation path $h_2 \to e$ will also be driven by the electric field (three-dimensional red arrow in Extended Data Fig. 5c). Hence, $p_k^{h_2 e} \propto d_{eh_2}E(t)$ initially has a linear dependence on the driving field. Eventually electrons from $h_2$ will be excited to the conduction band, which will create vacancies in $h_2$ and allow for transitions $h_1 \to h_2$ between the valence bands.

As soon as $h_1 \to h_2$ transitions (flat red arrow in Extended Data Fig. 5c) become possible, the second excitation path, described by the second term in equation (5), $p_k^{h_1 e}|_{\text{second}} \propto d_{h_2 h_1}E(t)p_k^{h_2 e}$, opens up. This path leads to a field induced excitation from the first valence band via the second valence band to the conduction band and is mediated by the polarization $p_k^{h_2 e}$. Thus only if a polarization $p_k^{h_2 e}$ is already present and the transition $h_1 \to h_2$ is possible, this indirect path exists. However, $p_k^{h_2 e}$ itself depends initially linearly on the electric field. Therefore, the indirect path $p_k^{h_1 e}|_{\text{indirect}} \propto d_{h_2 h_1}d_{eh_2}E(t)^2$ depends quadratically on the electric field and is proportional to the product of the transition dipole-matrix elements $d_{h_2 h_1}$ for $h_1 \to h_2$ and $d_{eh_2}$ for $h_2 \to e$. For strong excitations this quadratic dependence is replaced by a series of terms which are of even order in the driving field. Overall, the transition $h_1 \to h_2 \to e$ has an even symmetry with respect to the driving field.

Combining direct and indirect paths, the sum of their amplitudes—not their probabilities—defines the total transition yield. Therefore, in the lowest order, the total polarization

$$p_k^{h_1 e}|_{\text{total}} = p_k^{h_1 e}|_{\text{direct}} + p_k^{h_1 e}|_{\text{indirect}} \propto d_{eh_1}E(t) + d_{h_2 h_1}d_{eh_2}E(t)^2 \qquad (6)$$

consists of linear and quadratic contributions. For strong excitations, the field dependence is replaced by functions which are of even and odd order in the driving field. The resulting quantum interference controls the symmetry of the excitation $h_1 \to e$ because direct and indirect paths involve different field orders, as depicted by the red and blue arrows in Extended Data Fig. 5d. Therefore, changing the sign or the phase of the driving field $E(t)$ allows for direct control of the quantum properties of the excited state e. Equation (6) shows that all three transitions $h_1 \to e$, $h_2 \to e$, and $h_1 \to h_2$ are needed to produce quantum interference. If one transition $\lambda \to \lambda'$ is forbidden, that is, $d_{\lambda \lambda'} = 0$, $p_k^{h_1 e}|_{\text{total}}$ can only have one contribution with either even or odd parity in $E$.

Another contribution to the indirect path $h_1 \to h_2 \to e$ is described by the third term in equation (5), $p_k^{h_1 e}|_{\text{third}} = d_{eh_2}(k)E(t)p_k^{h_1 h_2}$. Here, the polarization between the two valence bands mediates the transition to the conduction band. However, $p_k^{h_1 h_2}$ is not driven by the electric field directly and may thus have a different field dependence compared to the $p_k^{h_2 e}$-mediated transitions, effectively creating an additional excitation path.

In the full five-band system, the additional bands will greatly increase the number of possible excitation paths. Even transitions involving three bands, for example, $h_1 \to h_2 \to h_3 \to e$, can become possible. The resulting excitation path will also contribute to the transition $h_1 \to e$ analysed above, leading to a quantum interference of at least three different excitation paths, with a possibly even more complicated field dependence. In the same way, excitations where the second valence band is the initial or final state, that is, $h_2 \to e$ and $h_2 \to h_1$, also contribute to the emission (direct paths).

**Perturbative versus non-perturbative quantum interference.** In principle, quantum interference could also be created in the perturbative regime. However, the frequency and intensity of the driving field would have to be chosen carefully to balance the involved excitation paths that depend on different orders of the driving field. A slight change in the properties of the pump field would then lead to a preferred path and, as a consequence, destroy the quantum interference effect since that preferred path would mainly contribute to the emission. As shown in the main text, the unipolar emission as a sign of quantum interference is observed for a variety of driving field strengths and central frequencies, which is a strong indicator for non-perturbative coherent control.

Owing to the very strong terahertz fields used in the experiments, the transition amplitudes are modulated by the electron occupations $f_k^\lambda$ of the involved states. The resulting massive dynamic occupation changes are beyond the validity of the perturbative analysis and the non-perturbative regime is reached. Technically, the

power-law dependence of transition amplitudes on the electric field $E$ is replaced by some nonlinear functions, denoted by $A_o(E)$ and $A_e(E)$ for direct excitations (for example, $h_1 \rightarrow e$) and indirect paths (for example, $h_1 \rightarrow h_2 \rightarrow e$), respectively. Nevertheless, as in the perturbative analysis, we can still identify an odd symmetry $A_o(-E) = -A_o(E)$ for the direct path and an even symmetry $A_e(-E) = A_e(E)$ for the indirect path. Also the superposition principle remains valid, implying proportionality $A_e(E) + A_o(E)$ for the total transition amplitude composed of the two excitation paths. The sign of the field thus controls the total outcome of the excitations, yielding $A_e(|E|) + A_o(|E|)$ for positive $E$ and $A_e(|E|) - A_o(|E|)$ for negative $E$. Therefore, the system described by equation (5) inherently contains non-perturbative coherent control via quantum interference. Note that, while being assigned direct and indirect paths, the excitation paths are true multi-photon transitions in the non-perturbative regime, not perturbative single and two-photon transitions.

**Interference path efficiency.** To determine the precise weight of direct versus indirect path contributions, we compare the total electron density, $n_{e_1}$, generated in the first conduction band with ($F_{cc} = 1$) and without ($F_{cc} = 0$) the indirect paths. We define $n_{e_1}$ 300 fs after the terahertz field, that is, at a time when most of the carrier generation has been completed. We then construct the interference path efficiency

$$\eta_{IPE} \equiv \frac{n_{e_1}(F_{cc}=1) - n_{e_1}(F_{cc}=0)}{n_{e_1}(F_{cc}=0)} \tag{7}$$

by computing the ratio of excess electrons created by the indirect paths ($n_{e_1}(F_{cc}=1) - n_{e_1}(F_{cc}=0)$) and only by the direct paths ($n_{e_1}(F_{cc}=0)$).

Extended Data Fig. 5e shows $\eta_{IPE}$ as a function of the terahertz field strength. For low $E_{THz}$, $\eta_{IPE}$ remains close to zero, indicating the dominance of the direct paths. Increasing the external driving field strength to 22 MV cm$^{-1}$ elevates $\eta_{IPE}$ to 50%. For $E_{THz} = 30$ MV cm$^{-1}$, the direct and the indirect paths reach the same efficiency ($\eta_{IPE} = 1$). In other words, non-perturbative excitations tend to balance the relative weights of the excitation paths, making interference effects strong, as described in the main text. We even observe that $\eta_{IPE}$ starts to decrease slightly, indicating a Rabi-flopping-type saturation, which is a unique hallmark of strongly non-perturbative excitations.

**Coherent control level.** Extended Data Fig. 6 shows the computed HH intensity envelopes as a function of the coherent control factor $F_{cc}$ as presented in Fig. 2c. However, all time traces are now displayed on the same absolute intensity scale. Including all transition paths ($F_{cc} = 1$) enhances the emission intensity by roughly 30 times, that is, more than simple two-path interference (maximum enhancement by a factor of four) predicts. This is indeed expected since switching off indirect transition channels ($F_{cc} = 0$) eliminates the contribution of multiple polarization combinations in the emission intensity, which lowers the HHG efficiency drastically. Additionally, GaSe has a particularly strong dipole matrix-element between the hole bands, as explained in ref. 41. This contribution is also missing when $F_{cc}$ is set to zero, together with multiple interference pathways. By closing the indirect transition channels in the $F_{cc} = 0$ calculation, the number of excited carriers is also reduced by a factor of two compared to the full calculation ($F_{cc} = 1$). As a combination of all these effects, $F_{cc} = 0$ yields a significant reduction in HHG, besides the qualitative difference in temporal emission, compared to the full computation.

**Minimal requirements for non-perturbative quantum interference.** In the main text, we have identified the following list of minimal conditions for the non-perturbative quantum interference:

(1) The system must have at least three states that are all mutually dipole coupled. The dipole transitions can then be illustrated in a triangle diagram, as shown in Extended Data Fig. 10a.

(2) The terahertz field must be non-resonant with each of the transitions because the excitation channels can otherwise not be balanced.

(3) The terahertz field must be strong enough to generate non-perturbative excitations where populations change within less than one oscillation cycle of the exciting field.

In the schematic of Extended Data Fig. 10a, circles denote three states (e, 1, and 2) coupled with three dipole-allowed paths (arrows). The actual dipole moment between any two states $\lambda$ and $\lambda'$ follows from

$$\boldsymbol{d}_{\lambda\lambda'} \equiv \frac{1}{\Omega} \int_\Omega dr^3 \phi_\lambda^*(\boldsymbol{r}) e \boldsymbol{r} \phi_{\lambda'}(\boldsymbol{r}) \tag{8}$$

where $\phi_\lambda(\boldsymbol{r})$ is the single-particle wave function of a given state $\lambda$. For solids, the integral can be performed over the unit-cell volume $\Omega$.

An inversion symmetric potential, depicted schematically in Extended Data Fig. 10b, produces single-particle eigenfunctions that have either even ($\phi_\lambda(-\boldsymbol{r}) = \phi_\lambda(\boldsymbol{r})$) or odd ($\phi_\lambda(-\boldsymbol{r}) = -\phi_\lambda(\boldsymbol{r})$) parity. Inserting these into

equation (8), $\boldsymbol{d}_{\lambda\lambda'}$ vanishes when both $\lambda$ and $\lambda'$ have the same parity and exists only between states with different parity. Since at least two out of the three states must have the same parity, an inversion symmetric system cannot form the required triangle system, making only $\Lambda$-, V- or ladder-transitions possible. Hence, the discovered non-perturbative quantum interference cannot be observed in inversion symmetric molecules or solids. More generally, inversion symmetric systems can have closed transition loops only among an even number of states, which always creates a total transition with odd symmetry with respect to the driving field. Inversion symmetric systems can therefore not exhibit the observed non-perturbative quantum interference even via more complex excitation paths. When the potential does not possess inversion symmetry as illustrated in Extended Data Fig. 10c, $\phi_\lambda(\boldsymbol{r})$ has neither even nor odd symmetry. Owing to the indefinite parity, $\boldsymbol{d}_{\lambda\lambda'}$ can exist between any combination of states, as is the case in GaSe. Solids or molecules lacking inversion symmetry can, thus, exhibit three states which are dipole-connected in a triangle configuration.

In Extended Data Fig. 10a, non-perturbative quantum interference can be realized in many different ways. One possibility is to choose $1 \rightarrow e$ to be the direct transition and $1 \rightarrow 2 \rightarrow e$ the indirect path (scenario QI1). Equivalently, the direct transition $2 \rightarrow e$ can interfere with the indirect path $2 \rightarrow 1 \rightarrow e$ (scenario QI2). To determine the interference conditions in these two cases, we apply $\phi_\lambda \rightarrow \tilde{\phi}_\lambda e^{i\theta_\lambda}$ in equation (8) and get $\tilde{d}_{\lambda\lambda'}$ with states $\tilde{\phi}_\lambda$ and $d_{\lambda\lambda'} = e^{i(\theta_{\lambda'} - \theta_\lambda)} \tilde{d}_{\lambda\lambda'}$. We choose $\theta_\lambda$ to produce real valued $\tilde{d}_{e1} = |\tilde{d}_{e1}|$ and $\tilde{d}_{e2} = |\tilde{d}_{e2}|$ while $\tilde{d}_{21}$ remains complex valued. As derived in equation (6), the overall strength of the QI1 transition scales with

$$\left| p_k^{1e} \right|_{QI1} \propto \left| \tilde{d}_{e1} E(t) + \tilde{d}_{21} \tilde{d}_{e2} E(t)^2 \right| = \tilde{d}_{e1} \left| E(t) + z E(t)^2 \right| \tag{9}$$

with $z \equiv \left| \frac{\tilde{d}_{e2}}{\tilde{d}_{e1}} \right| \tilde{d}_{21}$. Similar analysis for QI2 produces the expression within the absolute value in equation (9) with $z = \left| \frac{\tilde{d}_{e1}}{\tilde{d}_{e2}} \right| \tilde{d}_{12}$. Hence, both scenarios QI1 and QI2 lead to constructive (destructive) interference for a positive (negative) sign of the driving field and thus qualitatively contribute in the same way to the overall outcome of HH emission.

**Ultrashort pulse shaping.** The new cross-correlation scheme allows us to determine the exact timing with respect to the driving terahertz waveform as well as the intensity of the emitted HH bursts. The relative weight of HH bursts emitted at different half-cycles of the phase-stable waveforms can be controlled via the carrier-envelope phase (CEP) of the transients[5,31]: while continuously varying the CEP of the driving field, we observe that the individual peaks of the HH pulse train shift under a fixed envelope (Extended Data Fig. 8), defined by the envelope of the driving waveform. Quantum interference between more than two energy bands causes a pronounced polarity dependence of HH emission, leading to a temporal spacing of the HH bursts by the full driving period $T$ instead of $T/2$. This intrinsic property facilitates realization of isolated ultrashort field bursts even if the intensity envelope of the driving pulse is substantially longer than one half-cycle.

If the CEP changes by $\pi$ (Extended Data Fig. 8b) one may switch between one dominant HH pulse centred at the maximum field position (black curve) and two equally intense bursts corresponding to two positive driving half-cycles of equal field strengths (red curve). The direct CEP-controllability may thus allow for the generation of isolated ultrashort HH bursts as proposed in theoretical studies[6–8].

The flat spectral phase within single emission bursts of HHs favours the emission of extremely short optical pulses directly from the bulk semiconductor. Based on a semiclassical intraband calculation (supplementary information of ref. 5), we estimate that well-chosen spectral amplitude filtering could allow for the generation of 3-fs short bursts (Extended Data Fig. 9) without external pulse compression. Extending the subcycle pulse shaping techniques introduced in this study to higher frequencies by using wide-gap semiconductors as HH emitters may thus ultimately yield even subfemtosecond bursts from solid-state sources.

31. Sell, A., Leitenstorfer, A. & Huber, R. Phase-locked generation and field-resolved detection of widely tunable terahertz pulses with amplitudes exceeding 100 MV/cm. *Opt. Lett.* **33,** 2767–2769 (2008).
32. Eimerl, D., Davis, L., Velsko, S., Graham, E. K. & Zalkin, A. Optical, mechanical, and thermal properties of barium borate. *J. Appl. Phys.* **62,** 1968–1983 (1987).
33. Ruffin, A. B., Rudd, J. V., Whitaker, J. F., Feng, S. & Winful, H. G. Direct observation of the Gouy phase shift with single-cycle terahertz pulses. *Phys. Rev. Lett.* **83,** 3410–3413 (1999).
34. Gallot, G. & Grischkowsky, D. Electro-optic detection of terahertz radiation. *J. Opt. Soc. Am. B* **16,** 1204–1212 (1999).
35. Linden, S., Giessen, H. & Kuhl, J. XFROG — A new method for amplitude and phase characterization of weak ultrashort pulses. *Phys. Status Solidi B* **206,** 119–124 (1998).
36. Kane, D. J. Real-time measurement of ultrashort laser pulses using principal component generalized projections. *IEEE J. Sel. Top. Quantum Electron.* **4,** 278–284 (1998).

37. Wyatt, A. Frequency-resolved optical gating. http://www.mathworks.com/matlabcentral/fileexchange/16235-frequency-resolved-optical-gating-frog- (MATLAB central file exchange, 7 July 2008).
38. Kane, D. J. Recent progress toward real-time measurement of ultrashort laser pulses. *IEEE J. Quantum Electron.* **35,** 421–431 (1999).
39. Golde, D., Kira, M., Meier, T. & Koch, S. W. Microscopic theory of the extremely nonlinear terahertz response of semiconductors. *Phys. Status Solidi B* **248,** 863–866 (2011).
40. Schlüter, M. *et al.* Optical properties of GaSe and GaS$_x$Se$_{1-x}$ mixed crystals. *Phys. Rev. B* **13,** 3534–3547 (1976).
41. Segura, A., Bouvier, J., Andrés, M. V., Manjón, F. J. & Muñoz, V. Strong optical nonlinearities in gallium and indium selenides related to inter-valence-band transitions induced by light pulses. *Phys. Rev. B* **56,** 4075–4084 (1997).
42. Moiseyev, N. Selection rules for harmonic generation in solids. *Phys. Rev. A* **91,** 053811 (2015).
43. Kira, M. & Koch, S. W. *Semiconductor Quantum Optics* (Cambridge Univ. Press, 2011).
44. Golde, D., Meier, T. & Koch, S. W. Microscopic analysis of extreme nonlinear optics in semiconductor nanostructures. *J. Opt. Soc. Am. B* **23,** 2559–2565 (2006).
45. Schultze, M. *et al.* Attosecond band-gap dynamics in silicon. *Science* **346,** 1348–1352 (2014).
46. Vu, Q. T. *et al.* Light-induced gaps in semiconductor band-to-band transitions. *Phys. Rev. Lett.* **92,** 217403 (2004).
47. Schuh, K., Hader, J., Moloney, J. V. & Koch, S. W. Influence of many-body interactions during the ionization of gases by short intense optical pulses. *Phys. Rev. E* **89,** 033103 (2014).
48. Kira, M., Jahnke, F., Hoyer, W. & Koch, S. W. Quantum theory of spontaneous emission and coherent effects in semiconductor microstructures. *Prog. Quantum Electron.* **23,** 189–279 (1999).
49. Liu, Y.-W. in *Fourier Transform Applications* (ed. Salih, S.) 291–300 (InTech, 2012).
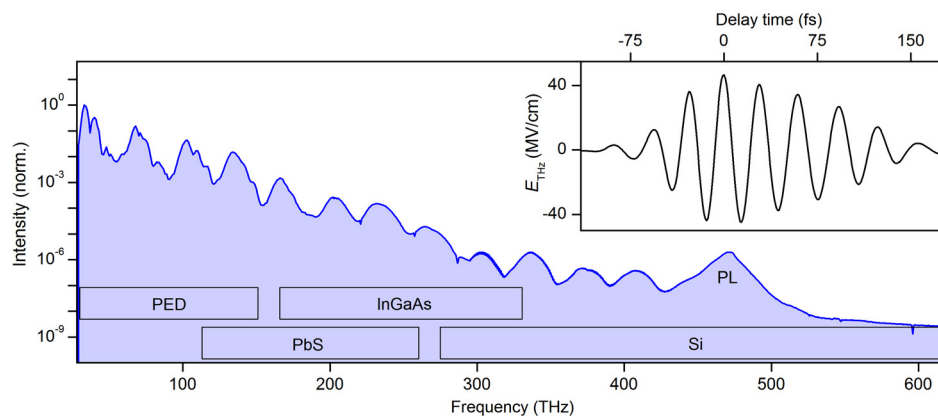
**Extended Data Figure 1 | High-order harmonic (HH) spectrum generated by intense phase-locked terahertz pulses in bulk GaSe.** The ultrabroadband HH emission is recorded using a monochromator with a calibrated pyroelectric detector (PED), a lead sulfide diode (PbS) and spectrometers employing InGaAs and cooled Si detectors. At a frequency of 476 THz interband photoluminescence (PL) dominates the spectrum. The driving multi-terahertz waveform is shown in the inset.
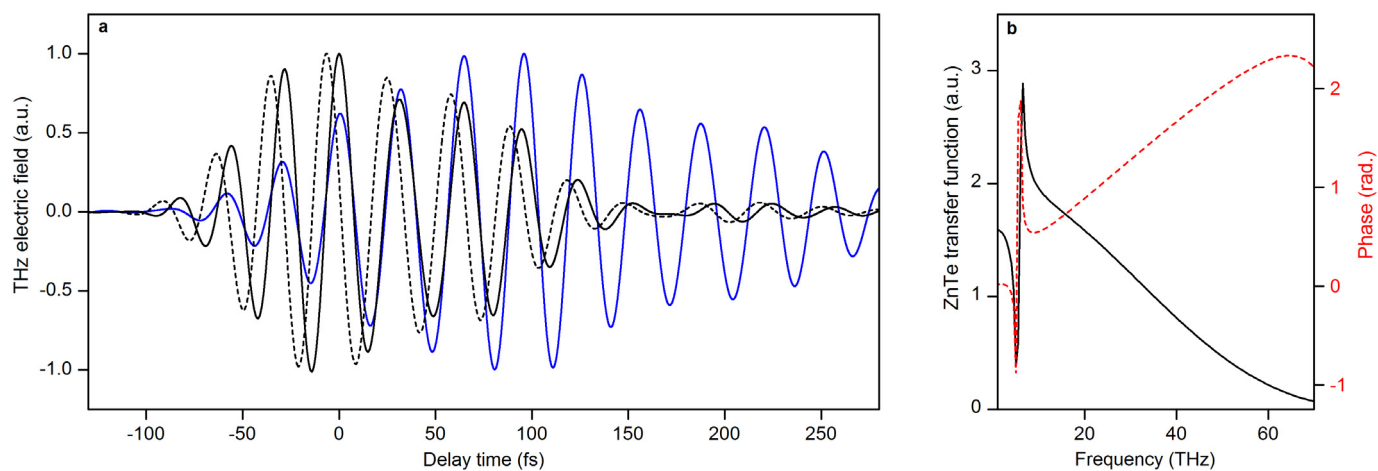
**Extended Data Figure 2 | Determination of the absolute timescale.**
**a**, Electro-optic signal of the multi-terahertz driving field as recorded using a BBO detector (thickness, 10 μm; blue curve, $S_{EOS\text{-}BBO}$) and a ⟨110⟩-oriented ZnTe crystal (thickness, 6.5 μm; black dashed curve, $S_{EOS\text{-}ZnTe}$) for spectral components between 12 and 45 THz. The black solid curve represents the corresponding terahertz electric field $E_{Det}$ as a function of delay time after correction for the complex-valued detector response of the ZnTe crystal displayed in **b**. **b**, Absolute value (black solid curve) and phase (red dashed curve) of the transfer function[34] calculated for a 6.5-μm-thick ZnTe electro-optic detector in the multi-terahertz frequency range.
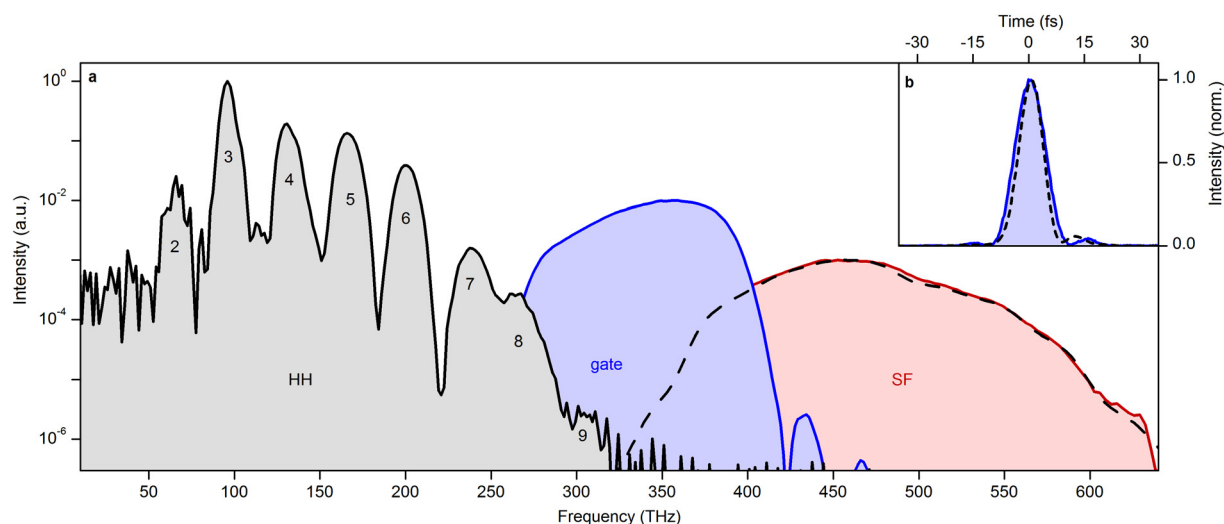
**Extended Data Figure 3 | Double-blind reconstruction of the experimental XFROG data. a**, Retrieved spectral intensities of the detected HH pulse sequence (grey, numerals indicate harmonic orders), the gating pulse (blue) and the sum-frequency intensity (SF) for optimal temporal overlap of gating and HH pulses (black dashed). All spectra displayed here correspond to the data set of main text Fig. 1. The measured spectral intensity of the sum-frequency signal is shown as a red shaded area for comparison. All spectra are normalized to their individual maximum and shifted in intensity for clarity. **b**, Temporal intensity profiles of the gating pulse as measured and reconstructed via SHG-FROG (blue) and double-blind XFROG (black dashed).
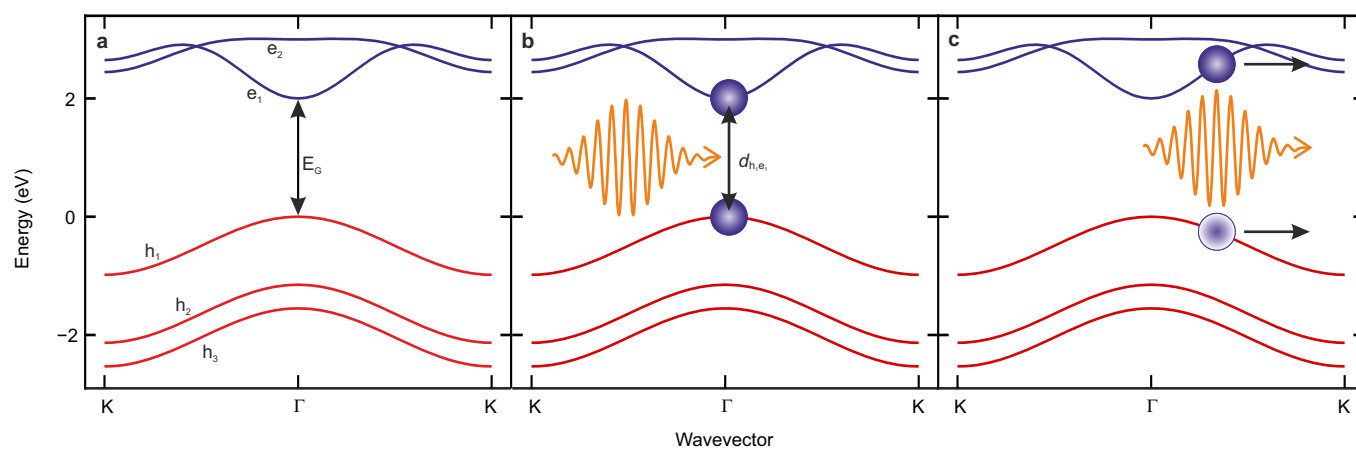
**Extended Data Figure 4 | Microscopic model. a**, Tight binding band structure of GaSe with three valence bands (red) and two conduction bands (blue). The bandgap $E_G$ is marked by the black arrow. **b**, Schematics of interband transitions. The external electric field (orange curve) stimulates a transition between electronic states (blue spheres) in different bands via the dipole moment $d_{h_1e_1}$, indicated by the black arrow. **c**, Schematics depicting intraband currents. Carriers (blue spheres) are accelerated by the external electric field (orange curve) inside their respective bands.
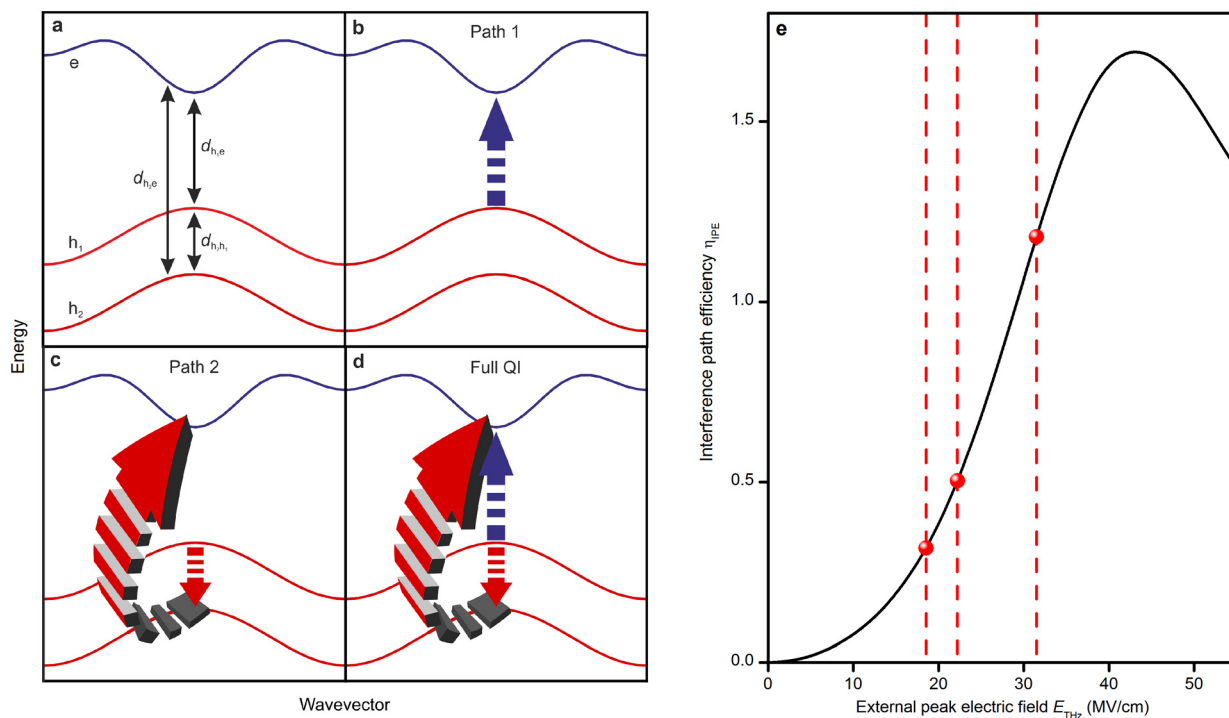
**Extended Data Figure 5 | Quantum interference paths.** **a**, Simplified band-structure schematics consisting of two valence bands $h_1$ and $h_2$ (red lines) and one conduction band e (blue line). The allowed transitions are labelled and marked by black arrows. **b**, Schematic of the direct excitation path. The transition $h_1 \rightarrow e$ is marked by the blue arrow. **c**, Indirect excitation path consisting of the transition $h_1 \rightarrow h_2$ (red arrow) and $h_2 \rightarrow e$ (three-dimensional red arrow). **d**, Full quantum interference (QI): combination of the direct

excitation path $h_1 \rightarrow e$ (blue arrow) and the indirect excitation path $h_1 \rightarrow h_2 \rightarrow e$ (red arrows). **e**, The interference path efficiency $\eta_{IPE}(E_{THz})$, black line, describes the fraction of additional carriers promoted to the conduction band $e_1$ by indirect paths such as $h_1 \rightarrow h_2 \rightarrow e$ as a function of the driving terahertz field strength. For the peak fields used in our calculations (indicated by dashed red lines), the strength of indirect excitations is of the same order of magnitude as the strength of direct excitations ($\eta_{IPE} \propto \mathcal{O}(1)$).
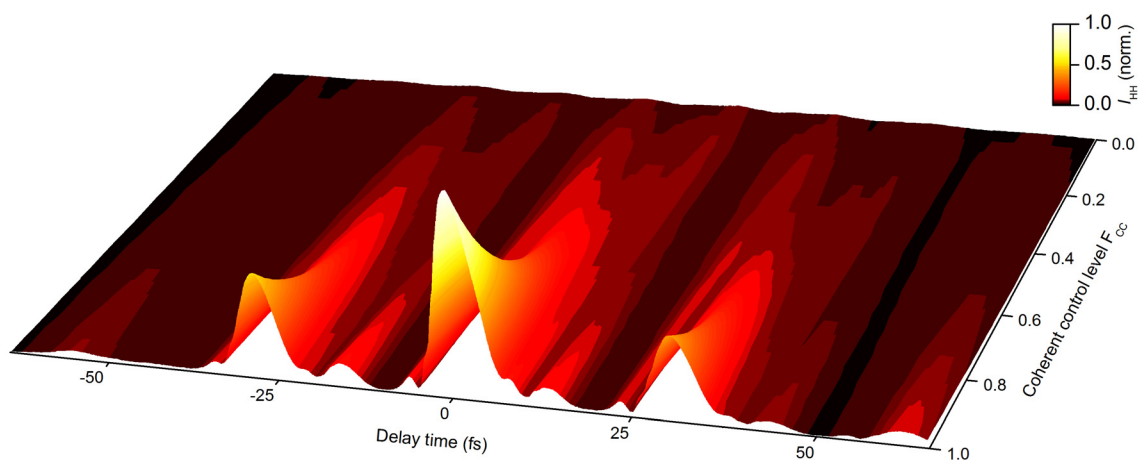
**Extended Data Figure 6 | Non-perturbative quantum interference.** Globally normalized HH intensity envelopes computed within the five-band model as a function of delay time and the coherent control factor $F_{cc}$ regulating coherent transitions between occupied valence bands. The same data are presented in Fig. 2c in normalized form. Bright colours mark strong emission, dark colours mark weaker emission (colour key at top right).
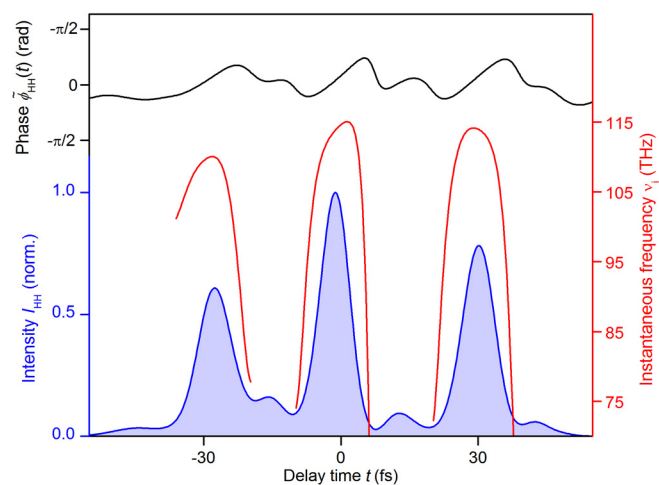
**Extended Data Figure 7 | Temporal phase of the HH emission from GaSe.** The black curve depicts the retrieved relative phase of typical HH bursts for driving peak fields of $33\,\mathrm{MV\,cm^{-1}}$. A trivial linear contribution to the phase representing the weighted central frequency $\nu_c$ of detected HHs within the detection bandwidth has been subtracted for better visibility: $\tilde{\phi}_{\mathrm{HH}}(t) = \phi_{\mathrm{HH}}(t) - 2\pi\nu_c t$. The intensity envelope $I_{\mathrm{HH}}$ (blue shaded area) and the derived instantaneous frequency $\nu_i$ of the three main HH pulses (red curves) are shown on the same timescale.
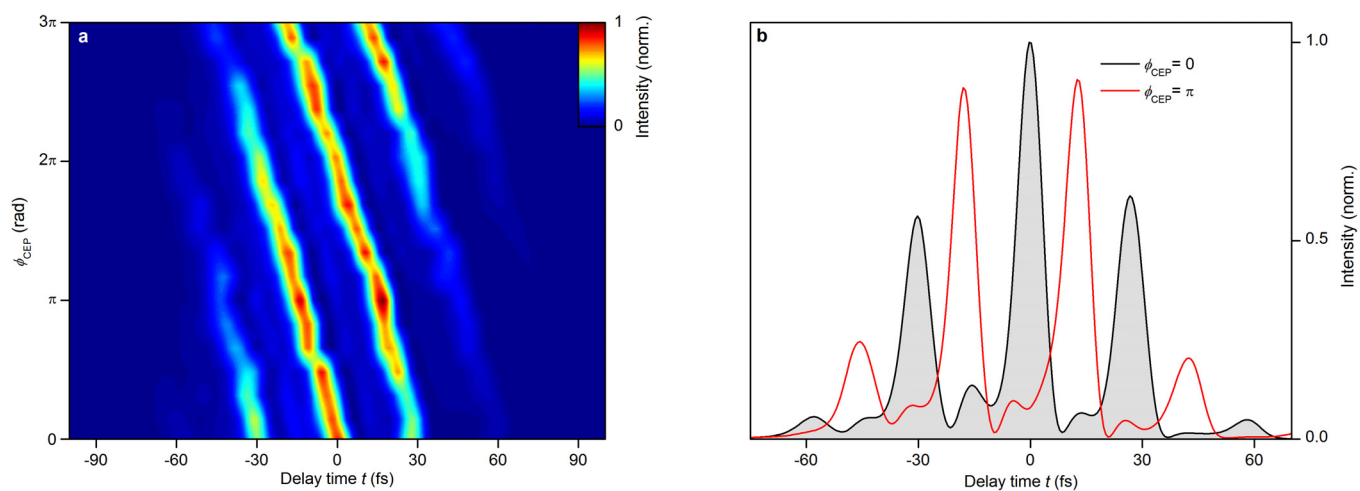
**Extended Data Figure 8 | HH pulse shaping via the CEP of the driving waveform. a**, False-colour plot of the reconstructed intensity envelopes of the HH pulse sequence versus delay time $t$ for different carrier-envelope phases $\phi_{CEP}$ of the driving waveform. **b**, Reconstructed HH intensity envelopes for $\phi_{CEP} = 0$ (black) and $\phi_{CEP} = \pi$ (red).
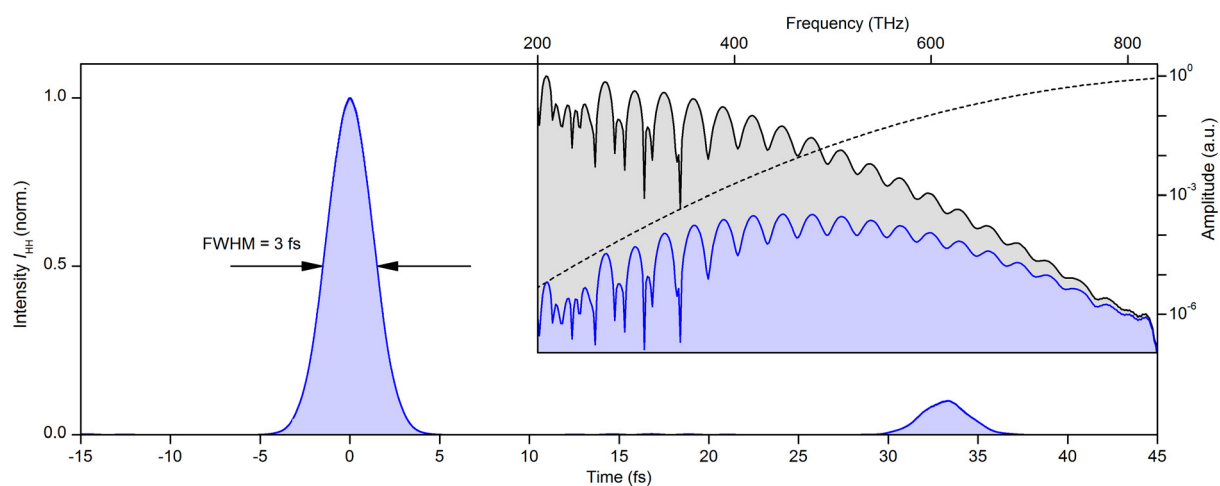
**Extended Data Figure 9 | Ultrashort pulse shaping via spectral amplitude filtering.** Intensity envelope (blue shaded area) of spectrally filtered HH bursts (inset, blue shaded spectrum) emitted from GaSe featuring a full-width at half-maximum of 3 fs only, as calculated with a semiclassical intraband model. Inset, calculated amplitude spectrum driven by a multi-terahertz transient with external peak fields of $43\,\mathrm{MV\,cm^{-1}}$ as emitted from the sample (grey shaded) and spectrally filtered (blue shaded) with a suitable high-pass filter (black dashed).
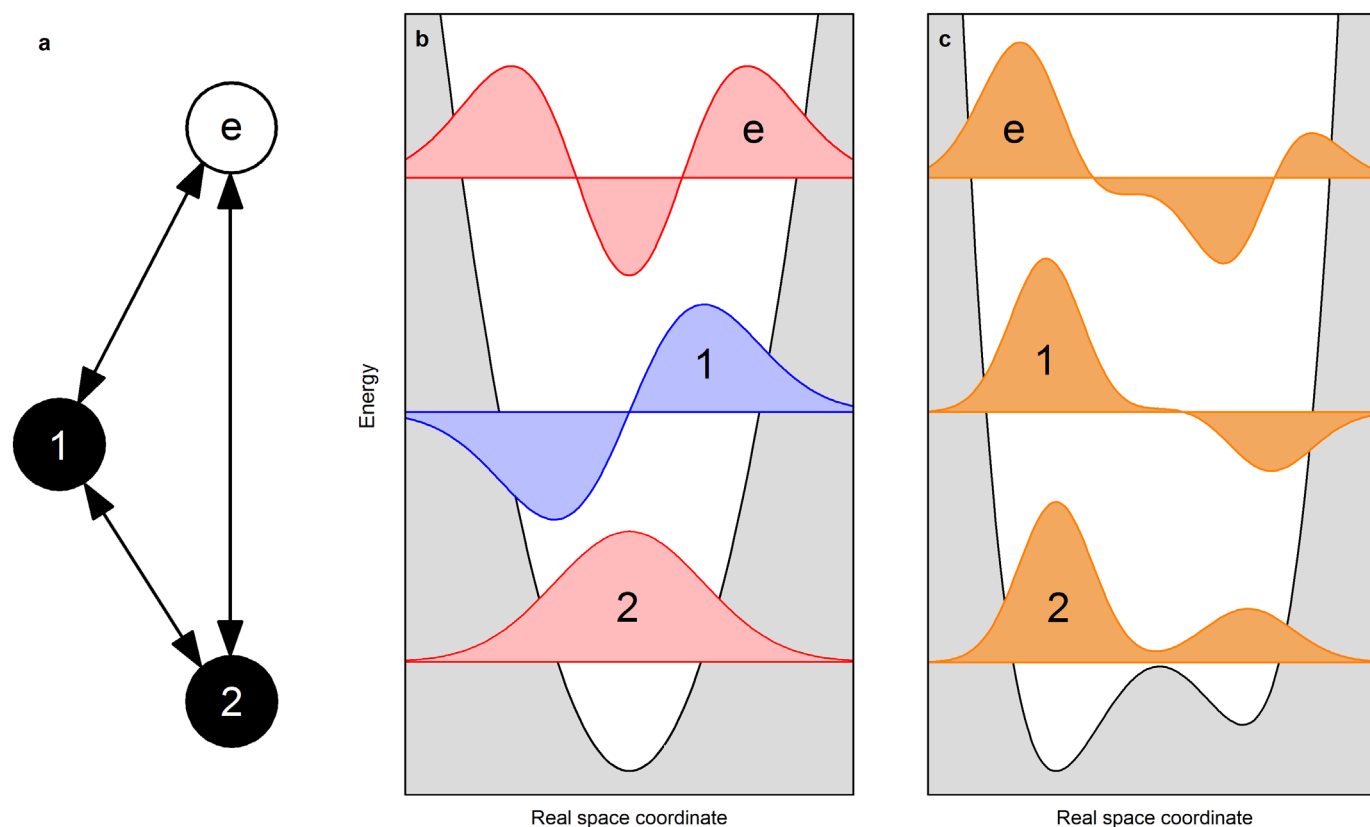
**Extended Data Figure 10 | Triangle system and symmetry. a**, Schematic of a triangle system of electronic states as a minimal condition for non-perturbative quantum interference. Filled circles 1 and 2 denote occupied states, whereas the sphere e symbolises an empty state. **b**, A symmetric potential (black solid line) and the resulting wave functions with even (red shaded area) and odd (blue shaded area) parity. **c**, System with an asymmetric potential (black line) resulting in wave functions with indefinite parity (orange shaded areas). See Methods for details.